OPEN ACCESS

Inorganic Materials ARTICLE

The Innovation Materials

Glass-like rare-earth doped fluoride single crystal for high repetition rate high energy lasers

Junyang Liu,[1,5,6] Junye Yang,[2,3,6] Hao Wu,[1,5] Yanyan Xue,[1] Zhen Zhang,[1] Qinghui Wu,[1] Dapeng Jiang,[1] Jie Chen,[2,3,*] Fengkai Ma,[4,*] and Liangbi Su[1,*]

*Correspondence: chenjie@ihep.ac.cn (J.C.); mafengkai@jnu.edu.cn (F.M.); suliangbi@mail.sic.ac.cn (L.S.)

Received: December 11, 2025; Accepted: May 6, 2026; Published Online: May 6, 2026; https://doi.org/10.59717/j.xinn-mater.2026.100217

GRAPHICAL ABSTRACT

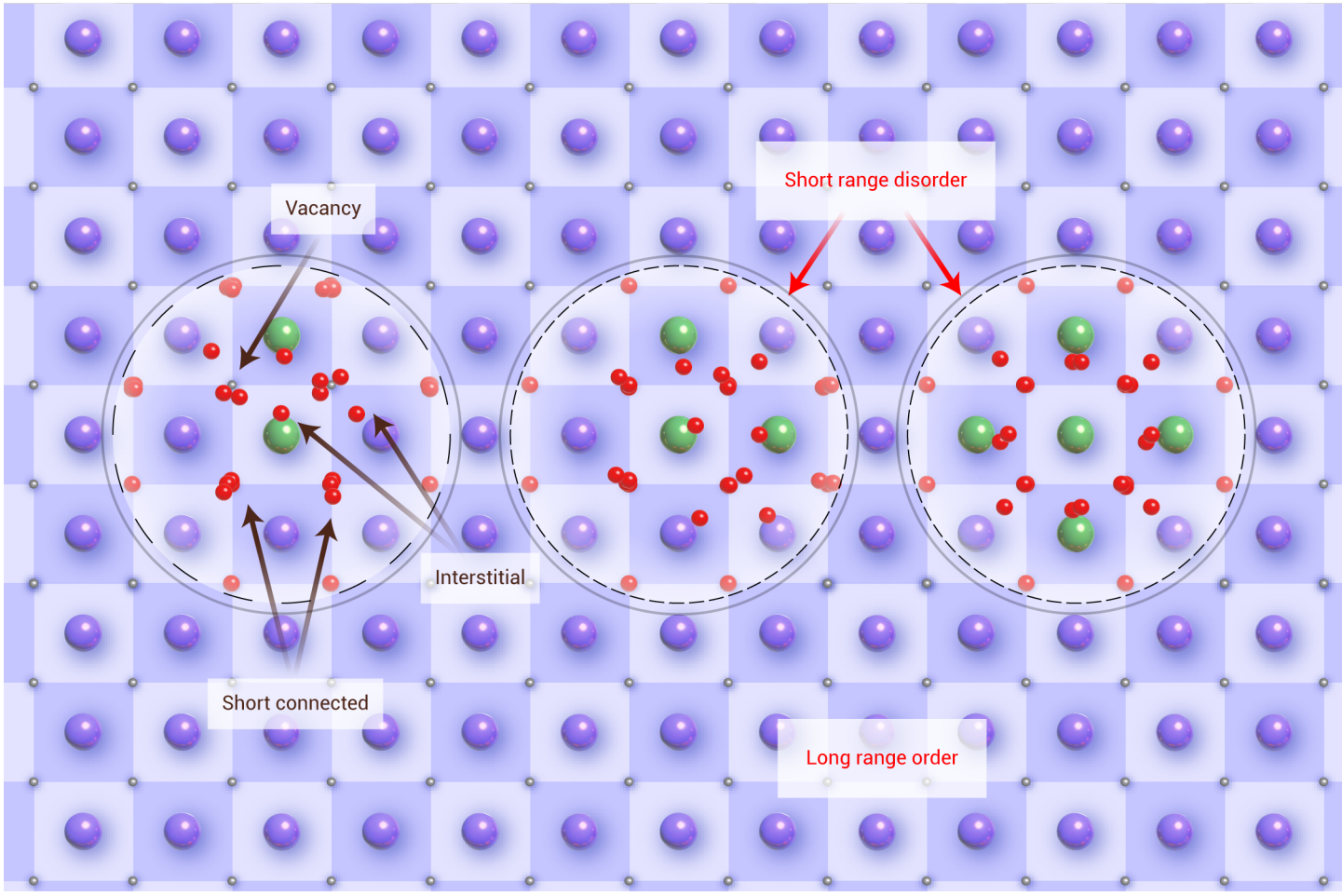

PUBLIC SUMMARY

- The glass-like structure with long-range ordered and short-range disordered is revealed in single crystal.
- Crystal with high thermal conductivity and broad bandwidth for high repetition rate ultra-fast laser is grown.
- Crystals range from low to high entropy doped with single element are revealed.

ARTICLE Inorganic Materials

www.the-innovation.org/the-innovation-materials

Glass-like rare-earth doped fluoride single crystal for high repetition rate high energy lasers

Junyang Liu,[1,5,6] Junye Yang,[2,3,6] Hao Wu,[1,5] Yanyan Xue,[1] Zhen Zhang,[1] Qinghui Wu,[1] Dapeng Jiang,[1] Jie Chen,[2,3,*] Fengkai Ma,[4,*] and Liangbi Su[1,*]

[1]State Key Laboratory of Functional Crystals and Devices, Shanghai Institute of Ceramics, Chinese Academy of Sciences, Shanghai 201899, China

[2]Institute of High Energy Physics, Chinese Academy of Sciences, Beijing 100049, China

[3]Spallation Neutron Source Science Center (SNSSC), Dongguan 523803, China

[4]Guangdong Provincial Engineering Research Center of Crystal and Laser Technology, Department of Optoelectronic Engineering, Jinan University, Guangzhou 510632, China

[5]Center of Materials Science and Optoelectronics Engineering, University of Chinese Academy of Sciences, Beijing 100049, China

[6]These authors contributed equally

*Correspondence: chenjie@ihep.ac.cn (J.C.); mafengkai@jnu.edu.cn (F.M.); suliangbi@mail.sic.ac.cn (L.S.)

Received: December 11, 2025; Accepted: May 6, 2026; Published Online: May 6, 2026; https://doi.org/10.59717/j.xinn-mater.2026.100217

Citation: Liu J., Yang J., Wu H., et al. (2026). Glass-like rare-earth doped fluoride single crystal for high repetition rate high energy lasers. *The Innovation Materials* **4**:100217.

Broad spectral bandwidth and high thermal conductivity are prerequisites for achieving high-repetition-rate ultrafast lasers. However, these properties are generally mutually exclusive and pose a persistent challenge in the field of laser materials. In this work, the reported rare-earth fluoride crystal is selected as laser gain materials. Through neutron diffraction, synchrotron radiation X-ray absorption spectroscopy and simulation calculations, a special structure with long-range order and short-range disorder in rare-earth-doped fluoride crystals is revealed for the first time. In the structure, anionic defects are randomly distributed around the activator ions, exhibiting glass-like disordered characteristics. The unique structure enables neodymium-doped fluoride crystals to reconcile the conflicting properties of broad spectrum and high thermal conductivity. Meanwhile, the successful growth of large-size crystals, coupled with the preliminary laser amplification, demonstrates that the developed neodymium-doped fluorites are promising candidates for high-repetition-rate ultrafast lasers.

INTRODUCTION

High-repetition-rate and high energy lasers, exhibiting high energy density, ultra-high-resolution, high-speed and high-precision micromachining, are driving transformative innovations across multidisciplinary frontiers, particularly in high energy for inertial confinement nuclear fusion ignition, compact laser-driven particle accelerators for broadband radiation sources, and femtosecond-resolved spectroscopy probing ultrafast dynamics in quantum materials and chemical reactions.[1-5] They have attracted widespread attention and great interest across diverse domains including strong-field physics, astronomy, biomedicine, energy, and information technology.[6] Consequently, the development of high-repetition-rate ultrafast laser sources assumes critical importance. Despite global research communities, especially in the main developed nations, including the United States, Japan, Russia and European Union, have made substantial investments in developing such systems, current technology still struggles to achieve an ultrafast light source at 10 Hz and even 100 Hz repetition rates.[7-10] The development of advanced gain media for the generation of high-repetition-rate and high energy lasers represents both the key bottleneck and primary target. For high-repetition-rate ultrafast lasers, laser gain media prerequisites include broad spectral bandwidths and high thermal conductivities to enable effective energy amplification and thermal management. For example, the rare earth-doped glass materials inherently exhibit broad photoluminescence bandwidths, which enables the generation of ultrafast pulses. The neodymium-doped glasses have demonstrated a 60 fs pulse and obtained optical parametric chirped-pulse amplification with petawatt-level output.[11,12] However, the insufficient thermal dissipation restricts the laser to single-shot mode.[13] The garnet crystals possess high thermal conductivities, which effectively suppresses thermal lensing distortion through active thermal management protocols. Due to the narrow emission bands, unfortunately, only picosecond pulses were generated.[14] The fundamental trade-off between broad emissions and high thermal conductivities constrained a persistent materials challenge in rare earth activated laser materials. Therefore, the primary challenge for the development of high-repetition-rate and high energy lasers critically hinges on advancing the development of novel laser materials with concurrently optimized spectral and thermal properties,[15] particularly with broad emission bandwidths while maintaining high thermal conductivities.

To address the management challenges, Yu et al. utilized diamond with high thermal conductivity as the heat sink, which significantly improved thermal transfer efficiency of the phosphor films.[16] However, the combination of diamond with bulk crystal progresses sluggishly due to the size limitations. Although nano/microstructural engineering in Nd^{3+}: Al_2O_3 has been demonstrated to significantly broaden emission bandwidths,[17] the design of microstructure in ceramics might be invalid for single crystal. Recently, the rare earth-doped alkaline earth fluoride crystals have aroused significant interests. The neodymium and yttrium co-doped fluoride crystal exhibits an ultrabroad spectral bandwidth coupled with superior thermal conductivities, which enables the generation of 103 fs pulses and laser amplification at 5 Hz repetition rate respectively.[18,19] In fact, the rare earth-doped fluorides synergistically integrate both broad spectral bandwidth and exceptional thermal conductivity, which contribute to the superior laser performance and render the crystals promising candidates for generation of high-repetition-rate ultrafast lasers. Despite six decades of research, the fundamental mechanisms underlying the coexistence of wide emissions and high thermal conductivities in rare earth-doped fluorides remain unresolved, constituting a persistent challenge in the fields. Though preliminary work attributed the broadening of the spectrum to rare-earth ion clusters, the specific structure formed remains undetermined.[20] Unraveling the microscopic structure within the crystal is a fundamental challenge that requires expeditious exploration.

In this work, the rare earth-doped fluoride crystals are investigated, and it is found that the crystals containing abundant anionic defects confined within the rare earth clusters generate a unique short-range disordered structure, yet preserving a macroscopically long-range ordered crystalline framework. The positionally disordered anions result in broad emissions due to the inhomogeneous effect.[21,22] The long-range ordered lattice facilitates efficient phonon propagation, leading to fast thermal dissipation.[23] The integration of long-range order and short-range disorder creates a structural paradigm that resolves the fundamental conflict between high thermal conductivity and broad spectral bandwidth in the lattice, enabling excellent and comprehensive laser performance. The first experimental observation of long-range ordered and short-range disordered structure removed the obstacle that persisted in the past six decades. The unique structure simultaneously opens an avenue for designing new high-repetition-rate ultrafast laser materials, which is highly expected to drive the breakthroughs in high-repetition-rate ultrafast laser technologies.

MATERIALS AND METHODS

Experimental section

Single crystals of $Ca_{1-0.006-y}Nd_{0.006}Y_yF_{2+0.006+y}$ (y = 0, 0.02, 0.05, 0.08, 0.10, 0.26, 0.32), $Ca_{0.7}Nd_{0.3}F_{2.3}$ and $Sr_{1-x}Nd_xF_{2+x}$ (x = 0.20, 0.30, 0.35, 0.40) were grown from the melt by the temperature gradient technique. Raw materials of NdF_3, YF_3, CaF_2, SrF_2 and PbF_2 with a purity of 4N were stoichiometrically weighted based on the stoichiometric ratios of the molar concentrations and well-mixed in an agate mortar. The homogeneous mixture was loaded into a graphite crucible. The growth process was in a vacuum with the chamber

pressure below 10^{-3} Pa. Following the program in ref. 24, the rate of crystal growth was 1.5 K/h. Then the growth process lasted for about ten days, after which the furnace underwent gradual cooling to room temperature. Finally, the as-grown crystals were obtained.

Near infrared absorption and emission spectra measurement

The crystals in seed part of the ingot were cut and prepared with dimensions of Φ11 × 2 mm^3 for the measurements. The sample was double-face polished for the near infrared absorption spectra measurement, which is executed at about 80 K. The Cary 5000 UV-Vis-NIR Spectrophotometer was utilized with a step of 0.1 nm, a spectral bandwidth of 0.3 nm and a dwell time of 0.5 s. The fluorescence spectra were recorded by FLS1000 time-resolved fluorimeter with a photomultiplier tube detector by liquid nitrogen.

Thermal conductivity characterization

The crystal was cut into 10 mm × 10 mm × 2 mm for specific heat capacity measurement in the laser thermal conductivity meter LFA 467. A 3.5 mm × 3.5 mm × 0.7 mm slice was then prepared for heat diffusion measurement in High-Temperature Specific Heat Tester MHTC96. Both samples were subjected to experimental determination in the temperature range 50 – 200°C. Thermal conductivity (λ) was determined by equation (1) based on the values of density (ρ), heat capacity (c) and the rate of heat diffusion (a).

$$\lambda = a \times \rho \times c \quad (1)$$

XRD and ICP-OES characterization

The crystal pieces were powdered and filtered with a 200-mesh sieve. The sieved powders, which were collected at room temperature by Rigaku Ultima-IV diffractometer (Japan), were used for the X-ray diffraction (XRD) measurement. The scan step was 0.02° and Cu Kα radiation was adopted as the beam. Data were collected in the range of 20 – 70° on 2θ scale. The powders were also used to measure the actual concentrations by inductively coupled plasma optical emission spectroscopy (ICP-OES). Powders with more than 5% rare earth concentrations were diluted to ensure the accuracy since the ICP-OES is suitable for measuring low concentrations.

NPD and XAFS spectra characterization

Neutron powder diffraction measurements were carried out on the energy-resolved neutron imaging instrument (ERNI) at China Spallation Neutron Source (CSNS). For the neutron experiments, the fine powder samples were placed in the Ti-Zr (null-scattering alloy) containers with a diameter of 9 mm and a height of 6 cm. The measurements were performed at room temperature. The NPD data were analyzed using the Rietveld package Z-Rietveld software,[25] aiming to best describe the peak profile yielded by different instruments.

XAFS spectra were collected at beamline BL11B and BL14W1 which is a wiggler-based beamline in Shanghai Synchrotron Radiation Facility. The measurement was carried out with a Si(111) double crystal monochromator and the experiment was performed at room temperature. The absorption spectra of Nd L_3-edge were then collected. Spectra data from $Ca_{1-0.006-y}Nd_{0.006}Y_yF_{2+0.006+y}$ crystals were measured in fluorescence mode while other samples with heavily doped concentrations were in transmission mode. The measurements were repeated three times, and the analysis of raw data was performed using ATHENA and ARTEMIS.[26] Based on the extracted polyhedrons, XANES spectra of Nd^{3+} L_3-edge were calculated with the FEFF code.[27] The Hedin-Lundqvist exchange-correlation potentials were used. The core hole states were treated with RPA screening. The calculated XANES spectra were then used as the standard models in the experimental XANES spectra fitting with the ATHENA code.

RESULTS

First, a schematic diagram of the long-range ordered and short-range disordered structure was elaborated. Typically, the anionic coordination structure surrounding the rare earth dopants in crystals is similar to the lattice structure of matrix, resulting in sharp emissions and high thermal conductivities.[28-30] However, the inherent long-range structural disorder in glass materials induces continuous variations in the local environments of rare earth, which contributes to broad emissions and poor thermal conductivities.[31-33] While for rare earth-doped fluoride crystal, it incorporates the merits of both crystals and glasses. As demonstrated in graphical abstract, a large number of interstitial fluorine atoms, fluorine vacancies and short connected anions were observed to be localized within the rare earth clusters, generating a short-range disordered anionic structure. Simultaneously, both the anionic framework outside cluster regions and the cationic framework remain highly ordered, preserving a long-range ordered crystalline structure. It is noted that the interstitial fluorines, short connected anions and fluorine vacancies do not belong to one specific lattice site. Their positions are randomly arranged around the rare earth ions. Consequently, the short-range disorder can be described as positional disorder. Additionally, through engineering the long-range ordered and short-range disordered crystal structure, we successfully made the laser crystal reconcile the conflicting requirements of broad emissions and efficient thermal transportation.

In order to illustrate the strategy in detail, the neodymium/yttrium doped calcium and strontium fluoride crystals were prepared. The X-ray diffraction (XRD) patterns confirm that the diffraction lines are in agreement with those of pure calcium and strontium fluorite crystals (Figures 1A & S1A). Even in crystals containing high dopant concentrations (32% Y^{3+} in CaF_2 and 40% Nd^{3+} in SrF_2), no impurity phases were detected. A remarkable feature of the alkaline earth fluoride crystals is their ability to accommodate a large number of trivalent rare earth ions without compromising the structure integrity.[34] The diffractions of (111) and (220) were fitted additionally using the single Lorentzian function.[35] Well agreement between the fitted and experimental lines confirms the preservation of single phase fluorite with long-range ordered structure across all samples (Figures 1B & S1B). Notably, the diffraction peaks of $Ca_{1-0.006-y}Nd_{0.006}Y_yF_{2+0.006+y}$ crystals shift to the left as the concentration rises, whereas almost no changes occurred in $Sr_{1-x}Nd_xF_{2+x}$ crystals. Since the ionic radii of Nd^{3+} (0.111 nm) and Y^{3+} (0.102 nm) are slightly smaller than that of Ca^{2+} (0.112 nm) yet much smaller than that of Sr^{2+} (0.126 nm),[36] it is difficult to have a reasonable explanation for the enlarged interplanar distances in CaF_2, as well as the unchanged distances in SrF_2 in view of cationic radius. In fact, the interstitial fluorine ions as charge compensations contribute to the enlarged sublattices,[37] which will be discussed further.

Though the anionic defects play a critical role in generating the structural disorder, their detailed characteristics remain unclear. Given that the light element fluorine is less sensitive to the X-ray detections, we referred to the neutron powder diffraction (NPD) studies to better clarify the microstructure. By Rietveld refinement on the diffraction data, detailed structural information, such as atomic positions, occupancy, etc., especially the content and position of fluorine, could be obtained. Figures 1C-J & S2 show the NPD patterns collected at room temperature together with the fitting results. The sharp diffraction lines also suggest the preserved long-range ordered fluorite type crystal structure. For the Rietveld refinement, the space group Fm-3m is employed, with cations at 4a (0,0,0) site and lattice fluorine, which we refer to as the 8c (0.25,0.25,0.25) site for the pure compound. By Rietveld analysis, we confirm the shortage of the lattice fluorine content, i.e. the fluorine vacancy (V_F) at 8c site. To further determine the position of interstitial fluorine, which is generated by the trivalent rare earth doping in the lattice, we tried different refinement models with extra fluorine located at 24e (x,0,0), 32f (x,x,x), 48i (0.5,y,y) and 48h (0,y,y). The refinements show that the interstitial fluorine tends to enter the 32f (F_{32f}) and 48i (F_{48i}) sites of the lattice, which is indicated by a slightly improved fitting and decreased χ^2 (Figure S3), consistent with the previous reports.[38,39] Fits with other models yield either negative occupancy values or positive values with considerable errors. Besides the results mentioned above which mainly focus on the long-range ion ordering, our analysis by neutron diffraction strongly indicates the presence of short-range correlated fluorine (Fshort) in the lattice. The theoretically calculated quantity of fluorine to maintain the electric neutrality of the lattice was obtained through neutron analysis. Additionally, the experimental results were obtained by summing up the quantities of fluorine at 8c, 32f, and 48i sites (Figure S4). The divergence between the theoretical and experimental quantities demonstrates the shortage of fluorine by considering only the long-range ordering. Since the valence states of Ca/Sr and Y/Nd are fairly stable with +2 and +3, respectively, the shortage of the long-range fluorine implies that part of fluorine ions locate at other positions without long-range ordering, i.e., with probably the short-range correlated state, which will be discussed further.

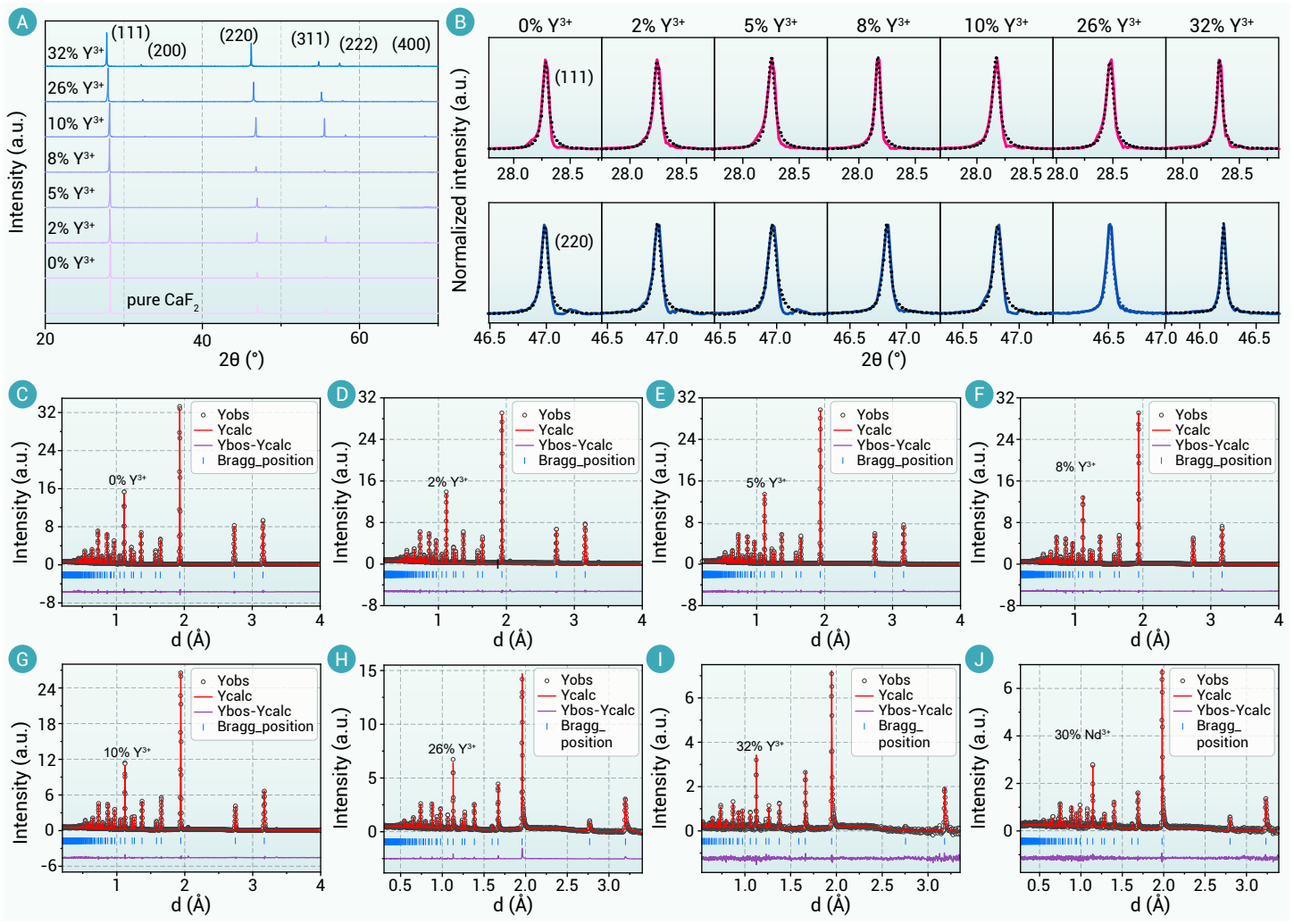

Figure 1. Crystal structures of the crystal (A) XRD patterns of $Ca_{1-0.006-y}Nd_{0.006}Y_yF_{2+0.006+y}$ crystals. (B) The single Lorentzian curve (dotted line) fitted diffraction peaks (111) and (220). (C-J) NPD patterns together with the Rietveld refinement results of samples $Ca_{1-0.006-y}Nd_{0.006}Y_yF_{2+0.006+y}$ and $Ca_{0.7}Nd_{0.3}F_{2.3}$.

The anionic defects obtained by refinements are summarized in Figure 2. It shows that both the contents and occupancy of the defects increase as the rare earth concentration rises. The fluorine defects in $Ca_{0.7}Nd_{0.3}F_{2.3}$ were compared with those of $Ca_{1-0.006-y}Nd_{0.006}Y_yF_{2+0.006+y}$ crystal, and show relatively smaller content, occupancy and number of ions at the same doping level. The results suggest that the rare earth ions could induce the formation of anionic defects in the fluorite crystal, with a higher concentration of rare earth ions leading to greater defect density. It should be noted here that the nominal rare earth concentrations were used in the refinement. Since the real concentrations almost linearly correlate with the doping concentrations (Figure S5), it is reasonable to use the nominal ones.

As is known, alkaline earth metal fluorides are in cubic fluorite structure. A simple cubic anionic sublattice is formed as framework, and the cations occupy the empty anionic sublattices alternatively. One half of the anionic sublattices are empty. When trivalent rare earth ion substitutes for divalent cation, the interstitial fluorine, occupying the empty anionic sublattice, is very close to the rare earth ions as charge compensation. Then electric dipoles would be formed and they could be connected in head-to-tail style. The rare earth clusters are therefore detected and it is found that they are easily clustering in the crystal.[40] It is the clusters that inevitably cause the generation of interstitial fluorine and lattice fluorine vacancies.[41,42] According to previous simulation results of rare earth clusters,[43,44] the contents of V_F, F_{32f} and F_{48i} in neodymium and yttrium mixed clusters in calcium fluorite were extracted, as well as the contents in the pure neodymium clusters and yttrium clusters. The yttrium concentration dependent contents of V_F, F_{32f} and F_{48i} in different clusters are depicted in Figure 3. The contents of V_F in $2|0|2|2_1$ and $3|0|1|3_1$ clusters are the smallest and remain unchanged, while those in $3|0|2|4_1$ and $4|0|2|4_1$ increase as the yttrium concentration rises. The contents of V_F in $5|0|8|5_1$ and $6|0|8|6_1$ are the highest. Combined with the refinement results of Figure 2A, the increased content of V_F suggests that the rare earth clusters would evolve from dimers to higher order ones as the yttrium concentration rises. The decreased contents of F_{32f} (Figure 3B) and increased contents of F_{48i} (Figure 3C) in $5|0|8|5_1$ and $6|0|8|6_1$ are in agreement with the results in Figure 2B, which shows that the site occupancy of F_{48i} increases faster than that of F_{32f} especially in high doping levels. The result further confirms the formation of higher order clusters. It should be noted that the vacancies in the clusters are primarily caused by the absence or displacement of lattice fluoride ions. Meanwhile, interstitial fluoride ions mainly consist of those surrounding rare-earth ions for charge compensation, and also include a small fraction of lattice fluoride ions that have migrated away from their original sites. The refinement results show that there is only one position value in a sample due to the average effect (Figure S6A). However, as shown in Figure 4A, the simulated results clearly indicate that there exists a distance range for the interstitial fluorine position, and the range becomes larger in higher order clusters. The wide range of position values increases the degree of disorder in local area, approaching that of glass materials. It is noted that the contents of V_F, F_{32f} and F_{48i} in Figure 3 are relatively small in the clusters without yttrium ions. Consequently, $Ca_{0.7}Nd_{0.3}F_{2.3}$ crystal exhibits lower defect contents compared to $Ca_{1-0.006-y}Nd_{0.006}Y_yF_{2+0.006+y}$ crystal with y equaling to 0.3.

Besides the interstitial fluorine ions and lattice fluorine vacancies, Fshort was also uncovered from the simulated clusters (Figure 4B). Compared with the interstitial fluorine ions, the relaxed distances of Fshort are small,[45] which

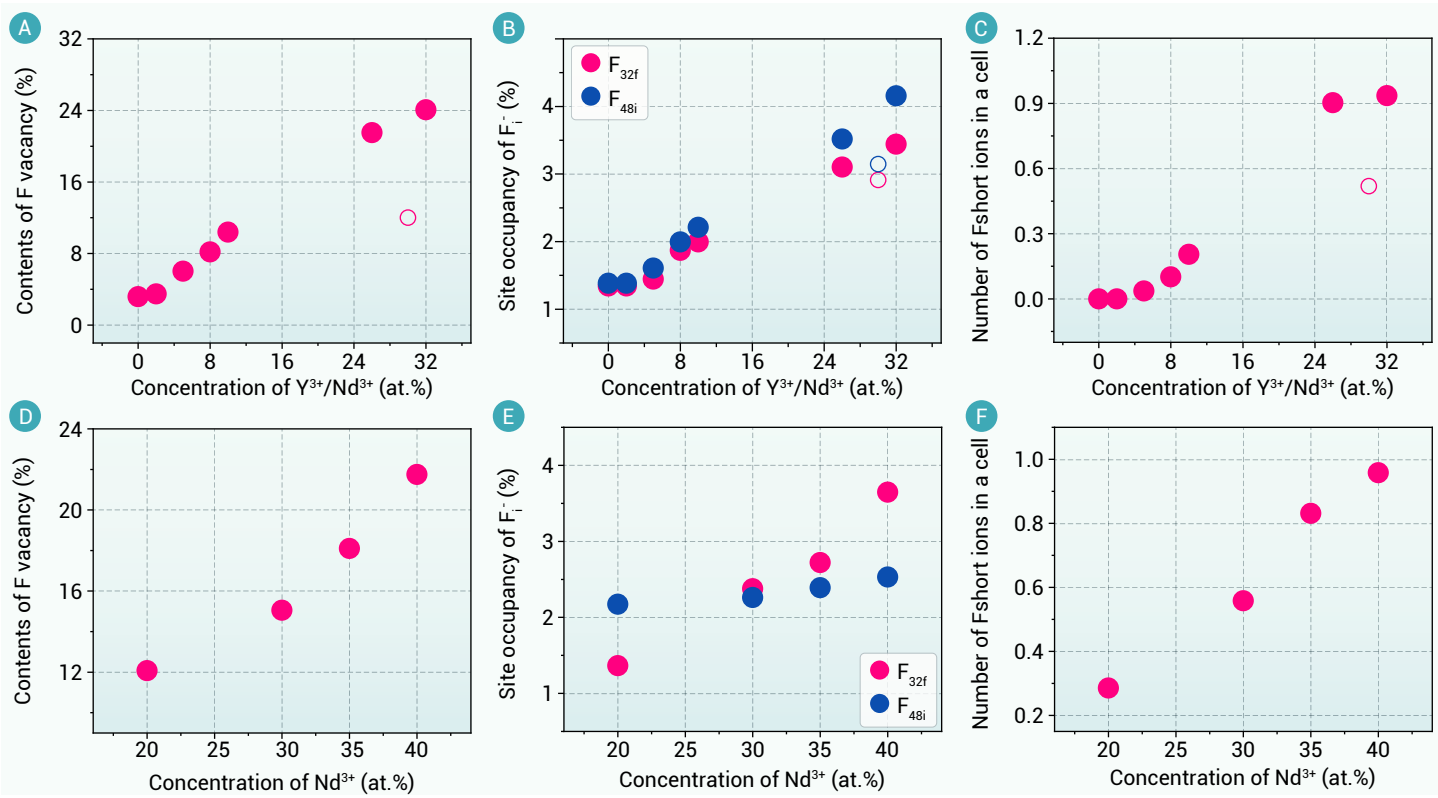

Figure 2. Anionic defects in the crystal (A-C) are respectively the rare earth concentration dependent contents of fluorine vacancy, site occupancy of interstitial fluorine, and number of Fshort in a cell of neodymium and yttrium codoped calcium fluorites, the hollow circle means that of $Ca_{0.7}Nd_{0.3}F_{2.3}$ crystal, and (D-F) are that in $Sr_{1-x}Nd_xF_{2+x}$ crystals.

means that they slightly deviate from the sites of lattice fluorine ions. In fact, simulations of the clusters demonstrate that under the combined influence of charge-compensating interstitial fluoride ions and trivalent rare-earth ions, lattice fluoride ions are irreversibly displaced from their original sites. A subset of ions covers a large displacement and becomes interstitial, while most remain close to their original sites with only a small displacement, resulting in a short-range and random distribution. And the number of Fshort increases as the clusters evolve into higher order ones. The large number of interstitial fluorine ions, short connected fluorine ions and fluorine vacancies leads to a diffuse background in the NPD (Figure 4C). A broad bump located around (d~ 2.2 Å) starts to emerge and gets stronger and stronger gradually as the concentration rises. For neutron diffraction or X-ray diffraction, usually a bump like that on the background implies sorts of short-range ordering in the lattice.[46] We consequently deduce the presence of Fshort in the lattice (Figure S7). The ionic defects in neodymium clusters of strontium fluorite were also investigated (Figures 4D-F). As can be seen, the content of V_F increases when it varies from low to high order clusters. The results suggest that more fluorine vacancies would be generated when more rare earth ions were introduced into the lattice, which is in agreement with the refinement results of Figure 2C. It also shows the contents of F_{32f} are higher than those of F_{48i} in the simulated neodymium clusters, which contributes to the larger site occupancy of F_{32f} in the crystal when doped with heavier concentrations (Figure 2D). Similarly, the positions of F_{32f} and F_{48i} are also not fixed values (insert of Figure 4E), as is the case with short range connected fluorine ions, which differs from the refinement results (Figures 2E, 3F & S6B). Then, a diffuse background was observed in the NPD (insert of Figure 4F).

The anionic defects in the neutron diffraction were qualitatively consistent with those of simulated rare earth clusters, and the rare earth clusters were found to evolve from low to high order structures. In this part, the synchrotron X-ray absorption fine structure (XAFS), which is sensitive to the microstructures of rare earth clusters, was applied. According to the simulated cluster structures, the polyhedrons of 9CN (coordination number) cubic, 10CN cubic, 8CN antiprism and 9CN antiprism, as representatives of cubic and square antiprism clusters, were extracted (Figure 5D).[43,44] Based on the multi-scattering theory and linear combination fitting method,[27] X-ray absorption near-edge structure (XANES) spectra of the polyhedrons were calculated and the experimental lines were fitted (Figures 5E-F & S8). The fitting results are depicted in Figures 5A-B. As can be seen, the contents of low order cubic sublattice centers decrease as the yttrium or neodymium concentration rises, while simultaneously, the contents of high order square antiprism clusters increase in $Ca_{1-0.006-y}Nd_{0.006}Y_yF_{2+0.006+y}$ and $Sr_{1-x}Nd_xF_{2+x}$ crystals. The structural evolutions from cubic sublattice to square antiprism structure, agree well with the neutron diffraction refinement. The results strongly indicate that the anionic defects are confined within the rare earth clusters. Interstitial fluorine, vacancies, and short connected fluorine defects within the clusters are randomly distributed around rare earth ions. The random distribution leads to severe lattice distortions in the anion lattice confined to these clusters, thereby forming a unique structure characterized by short-range disorder embedded within a long-range ordered framework.

To further confirm the random positional distribution of defects such as fluorine vacancies, interstitial fluorine, and short connected fluorine, the configurational entropy of the crystal is evaluated based on the neutron diffraction refinement results (see Supplementary).[47,48] As shown in Figure 5C, the configurational entropy increases with rising rare earth concentration. Notably, a high entropy state of 1.5 R is obtained even under single-ion doping conditions, with yttrium concentrations reaching 26% and neodymium levels exceeding 30% in $Ca_{1-0.006-y}Nd_{0.006}Y_yF_{2+0.006+y}$ and $Sr_{1-x}Nd_xF_{2+x}$, respectively. Only one type of rare earth ion induces the high entropy state. Since doping with individual rare earth ions induces the formation of defects such as vacancies, short connected fluorine arrangements, and interstitial fluorine, the random distribution of the defect sites generates additional configurational entropy. Thus it is the rare earth induced short-range disordered anionic lattice, that enables continuous tuning of configurational entropy. To sum up, doping with rare earth ions induces the formation of anion defects, whose randomly distributed positions lead the crystal to achieve a high-entropy state, which is consistent with the previously discussed results. In fact, not only fluorites, but also alkali halides and alkali-alkali earth halides exhibit numerous anionic defects under heterovalent substitution,[49,50] which shows a prospect to regulate the configurational entropy, as well as the locally disordered structures.

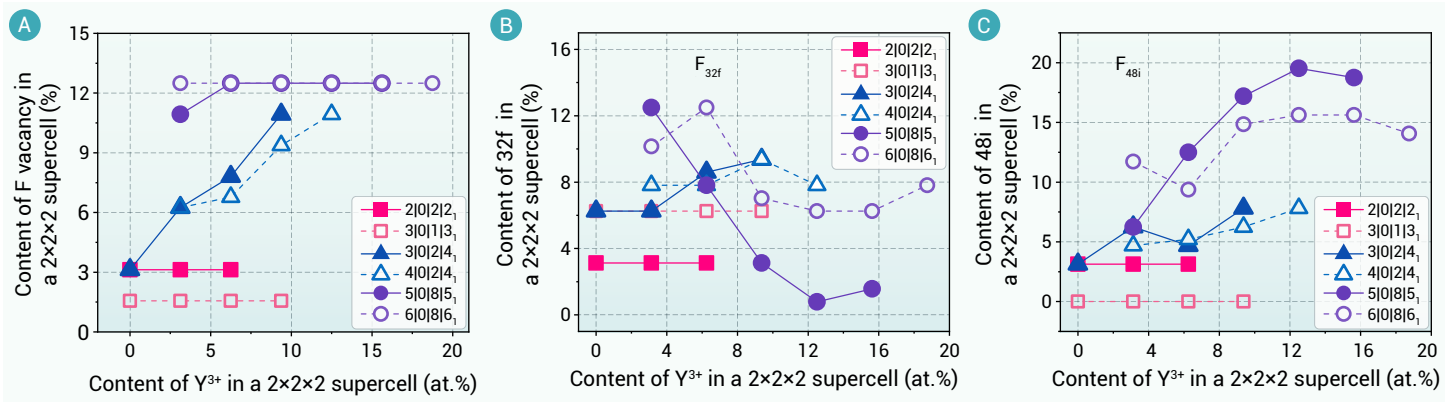

Figure 3. Simulated anionic defects in the crystal (A-C) are the yttrium concentration dependent contents of fluorine vacancy and interstitial fluorine at 32f and 48i Wyckoff site, respectively.

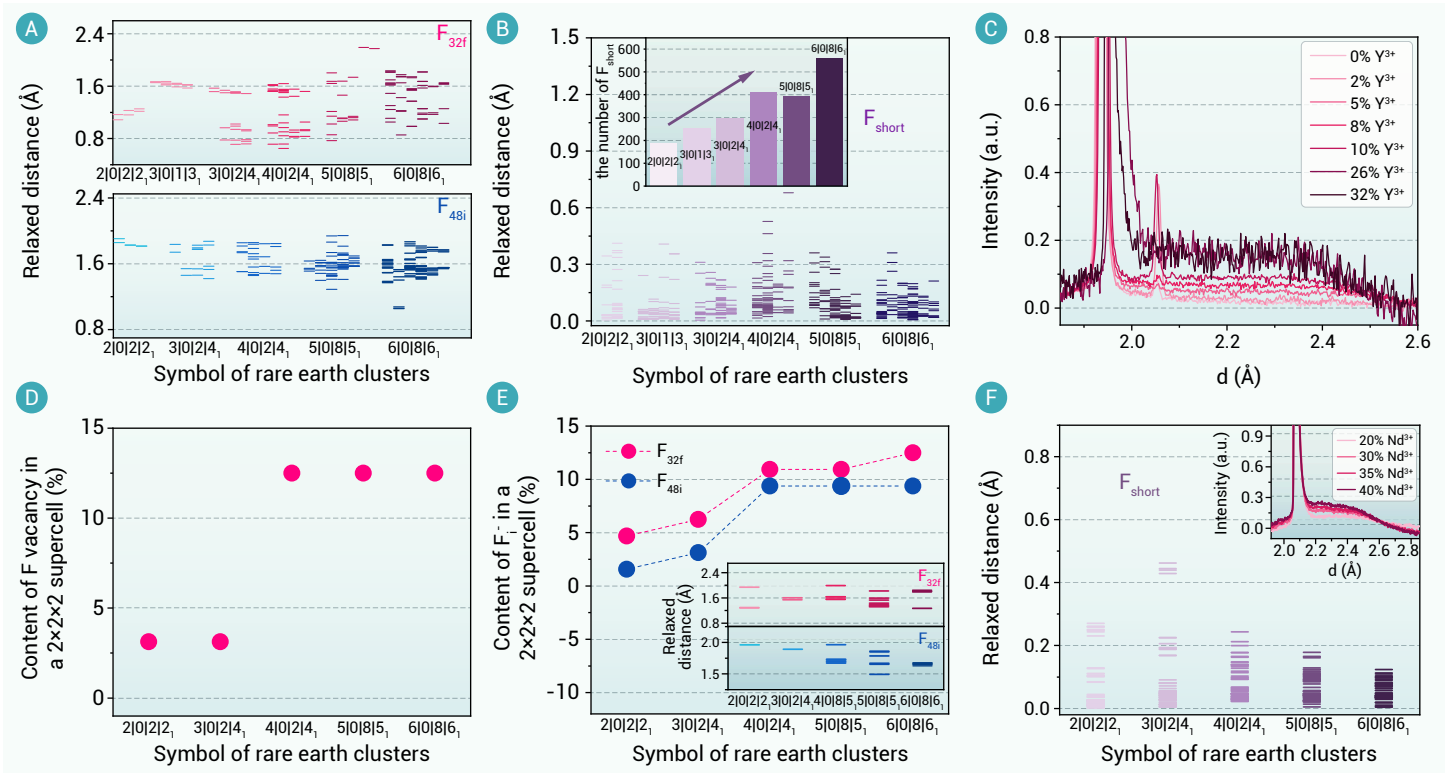

Figure 4. Location distribution of simulated anionic defects in the crystal and the background of neutron diffraction (A, B) The relaxed distances of 32f and 48i interstitial fluorine and short range connected fluorine in the rare earth clusters of calcium fluorite, respectively. The relaxed distance refers to the relative distance to the nearest lattice fluorine ion. The ions with relaxed distance smaller than a fifth of anionic sublattice side length were approximately adopted as short range connected fluorines.[45] The insert of (C) lists the number of short range connected fluorine ions in the cluster. The symbols of i|v|d|s, were used for the clusters, i the number of trivalent substitutional impurities, v the number of lattice anion vacancies, d the number of anions that deviated from the normal lattice site, s the number of interstitials at the nearest (r = 1) or next nearest site (r = 2).[61] (F) The NPD of $Ca_{1-0.006-y}Nd_{0.006}Y_yF_{2+0.006+y}$ crystal. (D, E) The contents of fluorine vacancy and 32f and 48i interstitial fluorine in the neodymium clusters of strontium fluorite, respectively. The insert in (E) is the relaxed distances of 32f and 48i interstitial fluorines. (F) The relaxed distances of short range connected fluorine in clusters of strontium fluorite, and the insert is NPD of $Sr_{1-x}Nd_xF_{2+x}$.

The short-range disordered structures not only contribute to high configurational entropy, but also result in broad emissions, serving as a critical feature for the generation of ultrafast pulses. The near infrared absorption and emission spectra, which serve as an intuitive demonstration, were measured and shown in Figures 6A-B & S9. As can be seen, the sharp peaks at about 790 nm become flatter and less intense with the addition of yttrium ions (black triangle in Figure 6A) when compared to the 4f → 4f sharp transitions. Concurrently, a significantly new broader absorption around 796 nm appears, exhibiting increased intensity (dotted line in Figure 6A). The yttrium concentration dependent absorption intensity agrees well with the XANES analysis in Figure 5A. It also shows that when the yttrium concentration exceeds 8%, the absorptions are almost identical (Figure 6A & S9A). The emission spectra of crystals doped with 10% and 32% yttrium are also nearly the same. Similar phenomena were observed not only in calcium fluorites, but also in strontium fluorites when doped with more than 10% neodymium, where the absorption spectra, as well as the emission spectra resemble one another (Figure 6B & S9B). The emission spectra of the lightly doped crystal are also almost the same as the crystal doped with much lower concentrations, 0.5% neodymium and 5% yttrium, which exhibit large emission bandwidths. In fact, the emission bandwidth owing to Nd^{3+} ions at a single site is only 0.8 nm,[28] whereas in phosphate glass, where Nd^{3+} ions can occupy multiple sites, inhomogeneous broadening allows the bandwidth to reach 25 nm. As previously mentioned, Nd^{3+} ions in fluoride crystals induce anion defects such as interstitial fluorine, fluorine vacancies, and short connected fluorine arrangements. These defect sites are randomly and locally distributed around the Nd^{3+} ions, forming a more diverse site structure

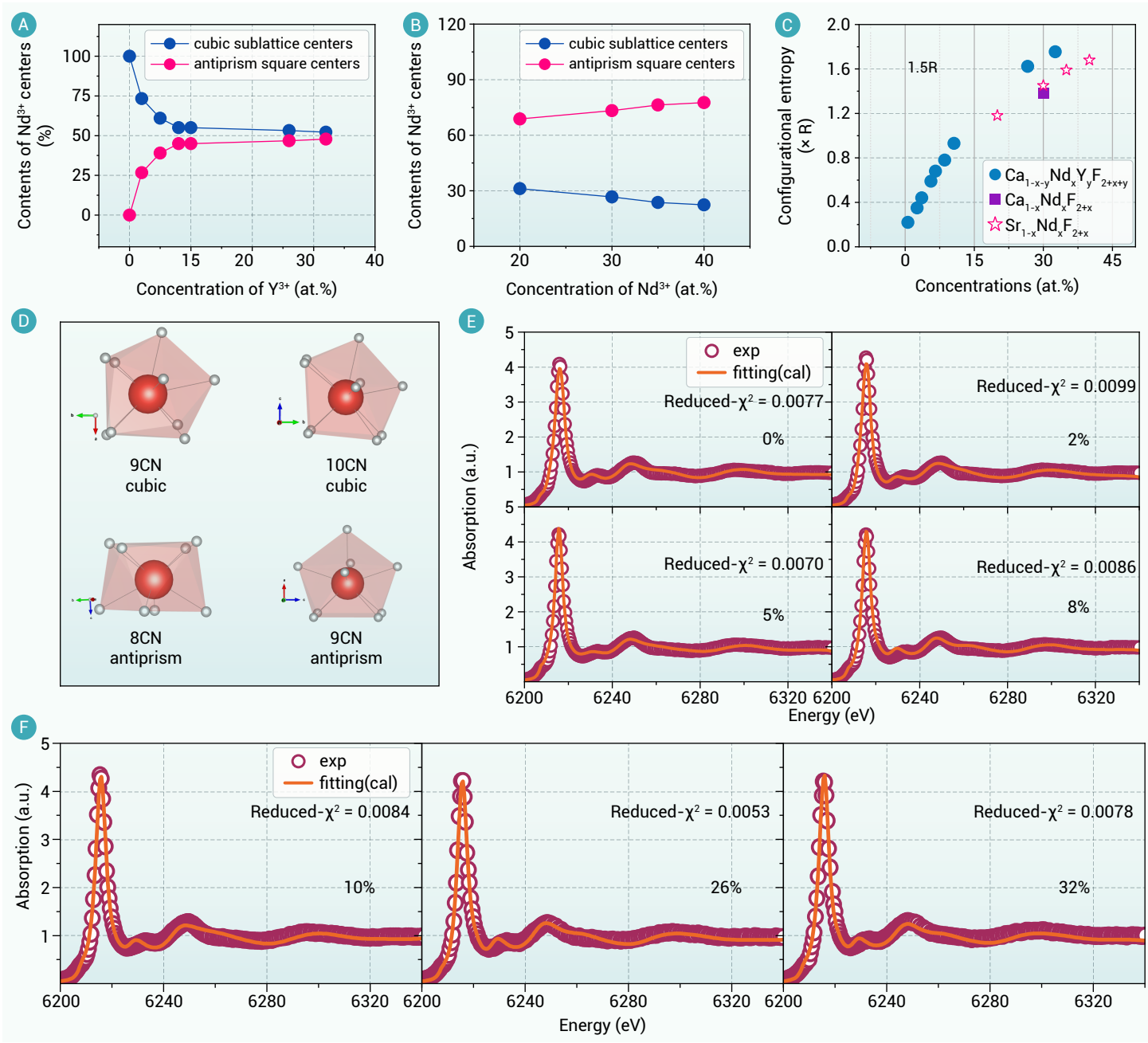

Figure 5. Evolution of the crystals (A, B) are respectively the rare earth concentration dependent contents of cubic sublattice and square antiprism structure in $Ca_{1-0.006-y}Nd_{0.006}Y_yF_{2+0.006+y}$ and $Sr_{1-x}Nd_xF_{2+x}$. (C) The concentration dependent configurational entropy of the fluorite crystal. (D) The polyhedron models for theoretical XANES spectra calculation. (E, F) The experimental XANES spectra and the fitting in $Ca_{1-0.006-y}Nd_{0.006}Y_yF_{2+0.006+y}$ crystals. The 9CN cubic and 10CN cubic represent the cubic sublattice clusters, and their coordination numbers are 9 and 10, respectively. The 8CN antiprism and 9CN antiprism represent the square antiprism structure clusters, and their coordination numbers are 8 and 9, respectively.

compared to that in Nd-doped glasses, which results in a broader emission bandwidth for the crystal than in Nd-doped glass. The lightly doped crystal has a larger emission bandwidth, and is comparable with that of Nd:glass.[31] Interstitial fluoride ions at different positions form diverse cluster structures with adjacent rare earth ions. When excited by light of single wavelength, the emission centers with various configurations produce slightly different central wavelengths in their emission spectra, which macroscopically manifest as an inhomogeneously broadened fluorescence spectrum. Therefore, with increasing doping concentration, the broader emission bandwidth indicates a greater diversity of cluster structures within the crystal. The results indicate that, despite differences in configurational entropy among these systems (Figure 5C), the degree of local structural disorder around the active ions in such crystals remains relatively consistent.

Compared with the heavy-doped samples, the crystals with low doping concentration show similar photoluminescence bandwidths and, more importantly, demonstrate superior thermal conductivities. As shown in Figure 6C, the thermal conductivity in calcium fluorite doped with 0.6% neodymium and 2% yttrium decreases with increasing temperature, which demonstrates a characteristic feature of crystalline materials. However, when the yttrium concentration reaches or exceeds 10%, the thermal conductivity increases with temperature, resembling that of glass materials.[51,52] Rare earth doping induces defects such as vacancies, interstitial fluorine atoms, and short connected fluorines. On the one hand, the positions of these defects are disordered, which strongly scatters phonons and significantly increases their mean free path. As a result, the thermal conductivity exhibits a glass-like temperature dependence of thermal conductivity.[53] On the other hand, the anion defects disrupt the integrity of the local lattice. The propagation of lattice vibrational waves is blocked by rare earth ions or clusters, leading to a

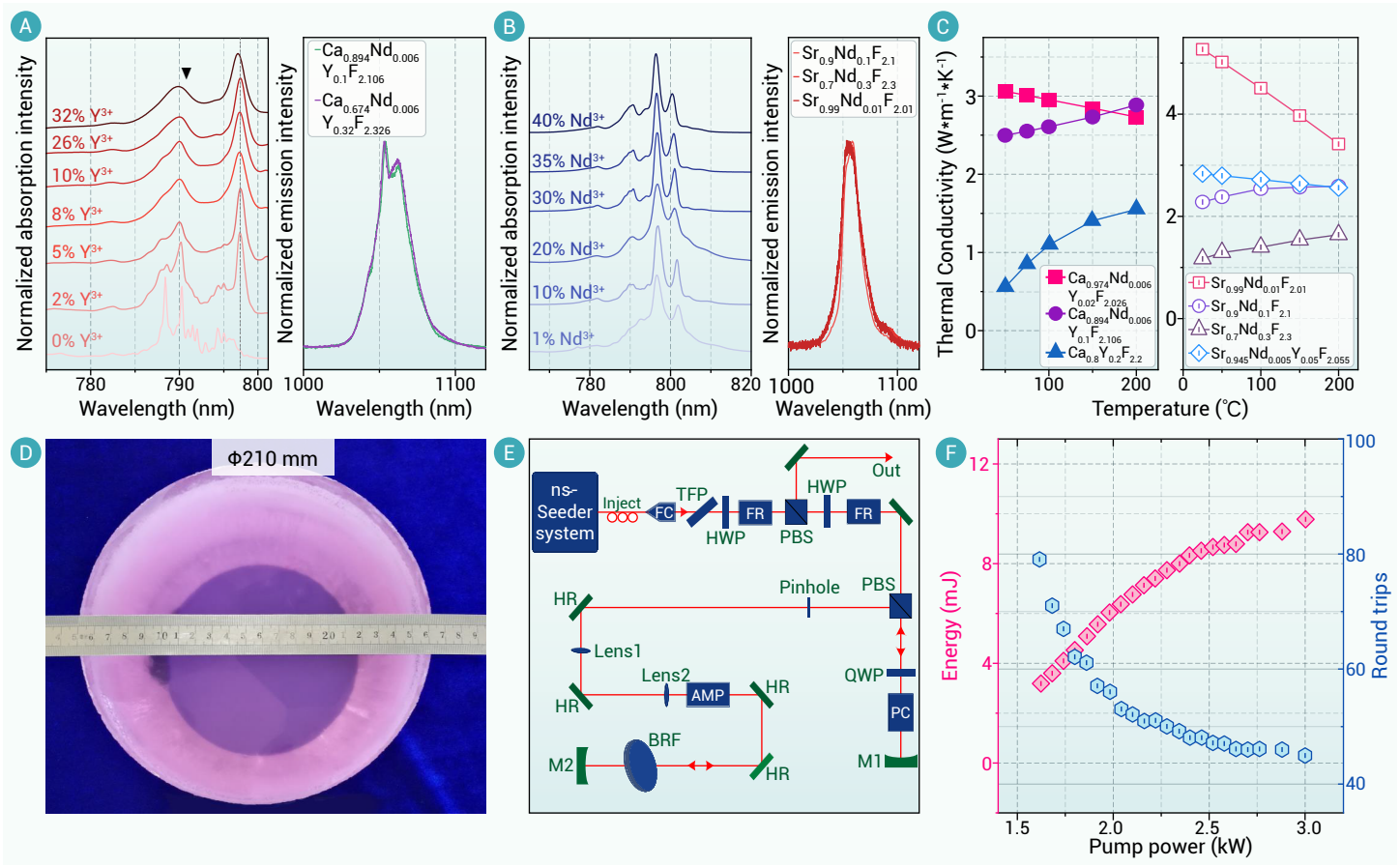

Figure 6. The spectral and laser performance of the crystals (A, B) The near infrared absorption and emission spectra of $Ca_{1-0.006-y}Nd_{0.006}Y_yF_{2+0.006+y}$, and $Ca_{0.7}Nd_{0.3}F_{2.3}$ and $Sr_{1-x}Nd_xF_{2+x}$, respectively. (C) The temperature dependent thermal conductivities of the crystal. (D) Graph of the as-grown crystal. (E, F) The amplification laser setup and the high repetition rate laser output, respectively.

marked decrease in thermal conductivity for crystals with high doping concentrations.[54] For instance, the thermal conductivity of a crystal doped with 20% Y is notably lower than that of one doped with 10% Y. Such behaviors were detected in strontium fluoride. The crystal doped with 1% neodymium exhibits relatively high thermal conductivity, which decreases with increasing temperature. When the doping concentration reaches 10% or higher, the thermal conductivity rises with increasing temperature. It is noted that for crystals doped with 5% yttrium or 10% neodymium, the thermal conductivities change minimally with temperature, and remain approximately constant. Due to the coupling of short-range disordered and long-range ordered structures, the temperature dependent thermal conductivity first decreases, then stabilizes, and eventually increases as the doping concentration rises, which reflects a transition from crystal-like to glass-like thermal transport. The characteristics further confirm that rare earth doping enables the generation of short-range disordered structures in the ordered fluoride lattice, producing single crystals that exhibit glass-like characteristics.

The high thermal conductivities in light-doped crystals also facilitate easier crystal growth. A strontium fluoride crystal doped with 0.5% neodymium and 5% yttrium was first prepared in large size (Figure 6D), free of scattering centers and streaks. The emission cross-section was evaluated to be 5.5×10^{-20} cm^2 and a fluorescence lifetime of 365 μs, which is comparable to commercial Nd-doped glasses.[31] Although the thermal conductivity of Nd-doped fluoride crystals is lower than that of Nd:YAG, Nd:YLF and Nd:YVO_4 crystals, the Nd-doped fluoride crystals far exceeds these materials as shown in Table 1. The bandwidth of Nd-doped fluoride crystals is comparable to that of Nd-doped glass. However, the thermal conductivity of Nd-doped fluoride crystals is 5.5 times higher than that of Nd-doped glass, which is highly conducive for high-repetition-rate ultrafast lasers. Based on the crystal, the laser performance was subsequently evaluated. The preamplification schematic diagram is shown in Figure 6E. After injecting the seed pulse with energy of around 1 nJ and pulse width of 5 ns into the regenerative amplifier, the output performance at a repetition rate of 10 Hz was collected. As can be seen in Figure 6F, the output energy increases as the pump power rises. At the same time, however, the number of round trips decreases. When the pump power reaches 3 kW, the maximum energy is 9.8 mJ. The horizontal and vertical beam quality factors of output were 1.18 and 1.23, respectively. Hence a laser output of 9.8 mJ at 10 Hz was finally achieved, which demonstrates a successful preliminary preamplification. Multi-stage amplification experiments with this crystal are in progress. With its combination of wide gain bandwidth, excellent thermal properties, and favorable four-level laser system, the Nd-doped fluoride crystal is highly expected to support extremely low-cost high repetition-rate high energy laser at room temperature directly. Considering that the neodymium-doped fluorites can be grown in large size, such crystals demonstrate significant potential in high-repetition-rate ultrafast laser technologies.

Table 1. Comparison of the emission bandwidth and thermal conductivity at room temperature of the neodymium-doped laser materials.

Laser materials	Bandwidth (nm)	Thermal conductivity ($W \cdot K^{-1} \cdot m^{-1}$)	Reference
Nd:YAG	0.9	7.9	28,29
Nd:YVO_4	1.1	5.1	57,58
Nd:YLF	1.4	6.0	59,60
Nd:glass	24	0.6	31,32
Nd,Y:SrF_2	25	3.3	this work

DISCUSSIONS AND CONCLUSIONS

As a common laser gain material, the spectral and laser properties of rare-

earth-doped fluoride crystal have been widely reported. Through the neutron diffraction, simulations and XAFS spectra, it is determined that the rare earth ions could induce numerous anionic defects, such as vacancies, interstitials and Fshort in alkaline earth fluorides, while maintaining the fluorite type crystal structure. These anion defects are localized within clusters, forming a discrete positional distribution. As the doping concentration is further increased, the content of anion defects rises, and consequently, the degree of lattice disorder localized around the rare earth ions also increases, which is corroborated by calculations of the configurational entropy. The stochastic arrangement of these anion defects induces the formation of short-range disordered structures. Such crystals, in which discrete distributions of anion defects around rare earth ions form short-range disorder within a long-range ordered lattice framework, are therefore referred to as glass-like crystals.

Doping with rare earth ions induces anionic defects in fluoride crystals, which are around rare earth ions. These exhibit a highly variable and disordered positional distribution. The scale of this local structural disorder is on the sub-nanometer level, indicating that no secondary phase is formed within the crystal, a result confirmed by XRD patterns (Figures 1 & S2)). Meanwhile, both XRD and neutron diffraction results verify that macroscopic, long-range ordered structure of the fluorite lattice is preserved. The combination of long-range order and short-range disorder structure enables rare-earth fluoride crystals to possess unique properties. On the one hand, anionic defects such as fluorine vacancies, interstitial fluorine, and short connected fluorine arrangements maintain the system in a high-entropy state, wherein significant changes occur in the electrical, mechanical, and other properties of the crystal. For example, the superionic conductive behavior of rare earth-doped fluoride crystals is strongly correlated with the type and content,[55] and rare earth doping significantly alters the superplastic deformation of fluoride crystals.[56] On the other hand, the locally disordered structures around the active ions lead to inhomogeneous broadening of the 4f → 4f sharp transitions, and broad absorptions and emissions were obtained, which supports the operation of ultrafast femtosecond pulses. Additionally, the long-range ordered lattice facilitates phonon propagation, enabling rapid heat dissipation. The high thermal conductivity is therefore observed in the rare earth-doped fluorite crystals, especially the light-doped ones. To sum up, the unique structure not only affects the spectral properties and thermal conductivity of crystal, but also holds potential for regulating other characteristics, such as ionic conductivity and plastic deformation.

Through the engineering of short-range disordered and long-range ordered structure, broad emissions and high thermal conductivities, inherently contradictory features, have been simultaneously achieved within a crystal. Broad bandwidth supports ultrafast laser output and high thermal conductivity enables efficient dissipation of operational heat in lasers while promoting scalable growth of bulk crystals. The availability of large-size crystals is very crucial for practical applications. It is the modification of this unique structure that we have achieved both broad band emission and high thermal conductivity simultaneously within the single crystal. The characteristic not only provides guidance for optimizing existing laser materials but also points to new directions for designing multifunctional crystals in the future. It should be pointed out that other parameters such as high gain, excellent optical uniformity, high laser-induced damage threshold, and stable thermomechanical properties are also crucial for the implementation of gain media in high-repetition-rate, high-energy laser systems. Consequently, these properties will be a primary focus for future research and optimization.

REFERENCES

1. Clark E., Krushelnick K., Zepf M., et al. (2000). Energetic heavy-ion and proton generation from ultraintense laser-plasma interactions with solids. *Phys. Rev. Lett.* **85**:1654. DOI:10.1103/physrevlett.85.1654
2. Huang K., Jin Z., Nakanii N., et al. (2024). Electro-optic 3D snapshot of a laser wakefield accelerated kilo-ampere electron bunch. *Light: Sci. Appl.* **13**:84. DOI:10.1038/s41377-024-01440-2
3. Meron O., Arieli U., Bahar E., et al. (2025). Shaping exciton polarization dynamics in 2D semiconductors by tailored ultrafast pulses. *Light: Sci. Appl.* **14**:80. DOI:10.1038/s41377-025-01748-7
4. Keller U. (2003). Recent developments in compact ultrafast lasers. *Nature* **424**:831–838. DOI:10.1038/nature01938
5. Fan J. J., Ou Z. Y. and Zhang Z. (2024). Entangled photons enabled ultrafast stimulated Raman spectroscopy for molecular dynamics. *Light: Sci. Appl.* **13**:163. DOI:10.1038/s41377-024-01492-4
6. Südmeyer T., Marchese S., Hashimoto S., et al. (2008). Femtosecond laser oscillators for high-field science. *Nat. Photonics* **2**:599–604. DOI:10.1038/nphoton.2008.194
7. Garanin S. G. and Krokhin O. N. (2011). High-power lasers and laser fusion. *Herald Russ. Acad. Sci.* **81**:204–210. DOI:10.1134/s1019331611030129
8. Temporal M., Canaud B., Garbett W. J., et al. (2014). Irradiation uniformity at the laser megaJoule facility in the context of the shock ignition scheme. *High Power Laser Sci. Eng.* **2**:e8. DOI:10.1017/hpl.2014.12
9. Niu S., Wang W., Liu P., et al. (2024). Recent advances in applications of ultrafast lasers. *Photonics* **11**:857. DOI:10.3390/photonics11090857
10. Li Y., Chen L., Chen M., et al. (2025). High-intensity lasers and research activities in China. *High Power Laser Sci. Eng.* **13**:e12. DOI:10.1017/hpl.2024.69
11. Aus der Au J., Kopf D., Morier-Genoud F., et al. (1997). 60-fs pulses from a diode-pumped Nd: Glass laser. *Opt. Lett.* **22**:307–309. DOI:10.1364/ol.22.000307
12. Gaul E. W., Martinez M., Blakeney J., et al. (2010). Demonstration of a 1.1 petawatt laser based on a hybrid optical parametric chirped pulse amplification/mixed Nd: glass amplifier. *Appl. Opt.* **49**:1676-1681. DOI:10.1364/ao.49.001676.
13. Yang S., Yin D., Gan Z., et al. (2020). Thermal effect of high energy repetition rate Nd:glass laser. *Chin. Opt. Lett.* **47**:0901004. DOI:10.3788/cjl202047.0901004
14. Maker G. and Ferguson A. (1989). Frequency-modulation mode locking of a diode-pumped Nd: YAG laser. *Opt. Lett.* **14**:788–790. DOI:10.1364/ol.14.000788
15. Norvig P., Relman D. A., Goldstein D. B., et al. (2010). 2020 visions. *Nature* **463**:26–32. DOI:10.1038/463026a
16. Yu Z., Zhao J., Yang Z., et al. (2024). A novel PiGF@ diamond color converter with a record thermal conductivity for laser-driven projection display. *Adv. Mater.* **36**:e2406147. DOI:10.1002/adma.202406147
17. Penilla E. H., Devia-Cruz L. F., Duarte M. A., et al. (2018). Gain in polycrystalline Nd-doped alumina: Leveraging length scales to create a new class of high-energy, short pulse, tunable laser materials. *Light: Sci. Appl.* **7**:33. DOI:10.1038/s41377-018-0023-z
18. Qin Z., Xie G., Ma J., et al. (2014). Generation of 103 fs mode-locked pulses by a gain linewidth-variable Nd, Y: CaF_2 disordered crystal. *Opt. Lett.* **39**:1737–1739. DOI:10.1364/ol.39.001737
19. Chen J., Peng Y., Zhang Z., et al. (2017). Demonstration of a diode pumped Nd, Y co-doped SrF2 crystal based, high energy chirped pulse amplification laser system. *Opt. Commun.* **382**:201–204. DOI:10.1016/j.optcom.2016.07.008
20. Kamat H., Wang F., Barnsley K. E., et al. (2021). Insight into the partitioning and clustering mechanism of rare-earth cations in alkali aluminoborosilicate glasses. *Chem. Mater.* **33**:7944–7963. DOI:10.1021/acs.chemmater.1c01352
21. Zhang Z., Ma F., Jiang D., et al. (2025). Laser crystals from combination paradigm to local structure design: A review on rational design principles, spectroscopic properties and laser applications. *Mater. Sci. Eng. R-Rep.* **162**:100869. DOI:10.1016/j.mser.2024.100869
22. Lu Y., Liu L., Gao R., et al. (2024). Ultrafast near-infrared pyroelectric detector based on inhomogeneous plasmonic metasurface. *Light: Sci. Appl.* **13**:241. DOI:10.1038/s41377-024-01572-5
23. Liu P., Zhao Y., Wang X., et al. (2024). Study on lattice dynamics and thermal conductivity of fluorite AF_2 (A= Ca, Sr, Ba) based on first principles calculations. *Phys. Chem. Chem. Phys.* **26**:10868–10879. DOI:10.1039/d4cp00201f
24. Yongzong Z. (1986). Growth of high quality large Nd: YAG crystals by temperature gradient technique (TGT). *J. Cryst. Growth* **78**:31–35. DOI:10.1016/0022-0248(86)90497-5
25. Oishi R., Yonemura M., Nishimaki Y., et al. (2009). Rietveld analysis software for J-PARC. *Nucl. Instrum. Methods Phys. Res., Sect. A* **600**:94–96. DOI:10.1016/j.nima.2008.11.056
26. Ravel B. and Newville M. (2005). *ATHENA, ARTEMIS, HEPHAESTUS*: Data analysis for X-ray absorption spectroscopy using *IFEFFIT*. *J. Synchrotron Radiat.* **12**:537–541. DOI:10.1107/s0909049505012719
27. Rehr J. J., Kas J. J., Vila F. D., et al. (2010). Parameter-free calculations of X-ray spectra with FEFF9. *Phys. Chem. Chem. Phys.* **12**:5503–5513. DOI:10.1039/b926434e
28. Sato Y. and Taira T. (2025). Augmented spectrum bandwidth of Nd-doped garnet and bixbyite by spectrum tailoring. *Opt. Express* **33**:24050–24059. DOI:10.1364/oe.554538
29. Wang B., Jiang H., Jia X., et al. (2008). Thermal conductivity of doped YAG and GGG laser crystal. *Front. Optoelectron.* **1**:138–141. DOI:10.1007/s12200-008-0049-6
30. Fan Z.-W., Qiu J.-S., Kang Z.-J., et al. (2017). High beam quality 5 J, 200 Hz Nd: YAG laser system. *Light: Sci. Appl.* **6**:e17004–e17004. DOI:10.1038/lsa.2017.4
31. Agnesi A., Greborio A., Pirzio F., et al. (2011). Femtosecond Nd: glass lasers pumped by single-mode laser diodes and mode locked with carbon nanotube or semiconductor saturable absorber mirrors. *IEEE J. Sel. Top. Quantum Electron.* **18**:74–80. DOI:10.1109/jstqe.2011.2104941
32. Naito K., Yamanaka M., Nakatsuka M., et al. (1992). Conceptual design studies of a laser diode pumped solid state laser system for the laser fusion reactor driver. *Jpn. J. Appl. Phys.* **31**:259. DOI:10.1143/jjap.31.259
33. Kuzmin A. A., Khazanov E. A., Kulagin O. V., et al. (2014). Neodymium glass laser with a phase conjugate mirror producing 220 J pulses at 0.02 Hz repetition rate. *Opt. Express* **22**:20842-20855. DOI:10.1364/oe.22.020842
34. Catlow C. R. A., Chadwick A. V., Greaves G. N., et al. (1984). Direct observations of the

dopant environment in fluorites using EXAFS. *Nature* **312**:601–604. DOI:10.1038/312601a0
35. Solari S. F., Poon L. N., Wörle M., et al. (2022). Stabilization of lead-reduced metal halide perovskite nanocrystals by high-entropy alloying. *J. Am. Chem. Soc.* **144**:5864–5870. DOI:10.1021/jacs.1c12294
36. Shannon R. D. (1976). Revised effective ionic radii and systematic studies of interatomic distances in halides and chalcogenides. *Acta Crystallogr., Sect. A: Found. Crystallogr.* **32**:751–767. DOI:10.1107/S0567739476001551
37. Cheetham A. K., Fender B. E. F. and Cooper M. J. (1971). Defect structure of calcium fluoride containing excess anions I. *Bragg scattering. J. Phys. C: Solid State Phys.* **4**:3107. DOI:10.1088/0022-3719/4/18/016
38. Hull S. and Wilson C. C. (1992). The defect structure of anion-excess $(Ca_{1-x}Y_x)F_{2+x}$ with x= 0.06. *J. Solid State Chem.* **100**:101-114. DOI:10.1016/0022-4596(92)90159-s.
39. Dudka A. P., Sobolev B. P. and Simonov V. I. (2013). Discovery of difference in the diffuse scattering from nonstoichiometric $Ca_{0.87}La_{0.13}F_{2.13}$ and $Ca_{0.92}Er_{0.08}F_{2.08}$ crystals with different types of clusters of structural defects. *Crystallogr. Rep.* **58**:822-828. DOI:10.1134/s1063774513060084
40. Lacroix B., Genevois C., Doualan J. L., et al. (2014). Direct imaging of rare-earth ion clusters in Yb:CaF_2. *Phys. Rev. B* **90**:125124. DOI:10.1103/physrevb.90.125124
41. Bevan D. J. M., Greis O. and Strähle J. (1980). A new structural principle in anion-excess fluorite-related superlattices. *Acta Crystallogr., Sect. A:Found. Adv.* **36**:889–890. DOI:10.1107/S0567739480001878
42. Krahl T., Scholz G. and Kemnitz E. (2014). Solid solutions CaF_2–YF_3 with fluorite structure prepared on the Sol–Gel route: investigation by multinuclear MAS NMR spectroscopy. *J. Phys. Chem. C* **118**:21066–21074. DOI:10.1021/jp505616f
43. Liu J., Wang Y., Zhang Z., et al. (2023). Insight into neodymium clusters and spectroscopic properties in CaF_2 single crystals. *Opt. Mater. Express* **13**:2288–2301. DOI:10.1364/ome.494068
44. Ma F., Zhou H., Tang Q., et al. (2022). Clusters modification for tunable photoluminescence in Nd^{3+}:SrF_2 crystal. *J. Alloys Compd.* **899**:162913. DOI:10.1016/j.jallcom.2021.162913
45. Sulyanova E. A., Karimov D. N. and Sobolev B. P. (2020). Nanostructured crystals of fluorite phases $Sr_{1-x}R_xF_{2+x}$ (R are rare-earth elements) and their ordering. 16: Defect structure of the nonstoichiometric phases $Sr_{1-x}R_xF_{2+x}$ (R= Pr, Tb–Yb) as grown. *Crystallogr. Rep.* **65**:560-565. DOI:10.1134/s1063774520040215
46. Danilkin S. A. (2009). Diffuse scattering and lattice dynamics of superionic copper chalcogenides. *Solid State Ionics* **180**:483–487. DOI:10.1016/j.ssi.2008.06.012
47. Liu Z. Y., Liu Y., Xu Y. J., et al. (2023). Novel high-entropy oxides for energy storage and conversion: From fundamentals to practical applications. *Green Energy Environ.* **8**:1341–1357. DOI:10.1016/j.gee.2023.04.007
48. Salian A. and Mandal S. (2022). Entropy stabilized multicomponent oxides with diverse functionality–a review. *Crit. Rev. Solid State Mater. Sci.* **47**:142–193. DOI:10.1080/10408436.2021.1886047
49. Ma X., Ding B., Yang Z., et al. (2024). Sulfur-vacancy-engineered two-dimensional Cu@SnS_{2-x} nanosheets constructed via heterovalent substitution for high-efficiency piezocatalytic tumor therapy. *J. Am. Chem. Soc.* **146**:21496–21508. DOI:10.1021/jacs.4c04385
50. Mi J., Chen L., Ma J., et al. (2024). Defect strategy in solid - state lithium batteries. *Small Methods* **8**:2301162. DOI:10.1002/smtd.202301162
51. Popov P., Fedorov P. and Osiko V. (2014). Thermal conductivity of single crystals of the $Ca_{1-x}Y_xF_{2+x}$ solid solution. *Dokl. Phys.* **59**:199–202. DOI:10.1134/s1028335814050036
52. Kotrbová L., Uhlířová T., Pabst W., et al. (2025). Thermal conductivity of silica refractories and its temperature dependence during thermal cycling, compared to silicite and sandstone. *Open Ceram.* **21**:100735. DOI:10.1016/j.oceram.2025.100735
53. Nolas G. S., Wang D. and Beekman M. (2007). Transport properties of polycrystalline Mg2Si1-ySby (0≤y<0.4). *Phys. Rev. B* **76**:235204. DOI:10.1103/PhysRevB.76.235204
54. Toberer E. S., Baranowski L. L. and Dames C. (2012). Advances in thermal conductivity. *Annu. Rev. Mater. Res.* **42**:179-209. DOI:10.1146/annurev-matsci-070511-155040
55. Liu Y., Zhang Z., Yan X., et al. (2025). Highly efficient atomic-scale design of CaF_2 for ultrafast fluoride-ion conduction. *J. Mater. Chem. A.* **13**:24656-24664. DOI:10.1039/D5TA01953B
56. Zhang Z., Tan L., Zhou Y., et al. (2025). Anisotropic plasticity and fracture mechanisms of single-crystal CaF_2 under indentation: Insights from crystal plasticity simulation and experiment. *J. Mater. Res. Technol.* **39**:6435-6447. DOI:10.1016/j.jmrt.2025.11.003
57. Sato Y. and Taira T. (2005). Comparative study on the spectroscopic properties of Nd:$GdVO_4$ and Nd:YVO_4 with hybrid process. *IEEE J. Sel. Top. Quantum Electron.* **11**:613–620. DOI:10.1109/jstqe.2005.850569
58. Matthews D. G., Boon J. R., Conroy R. S., et al. (1996). A comparative study of diode pumped microchip laser materials: Nd-doped YVO_4, YOS, SFAP and SVAP. *J. Mod. Opt.* **43**:1079–1087. DOI:10.1080/09500349608233268
59. Wetter N. (2013). Neodymium doped lithium yttrium fluoride (Nd:$YLiF_4$) lasers. Handbook of solid-state lasers (Elsevier). pp:323-340. DOI:10.1533/9780857097507.2.323
60. Koechner W. (2013). Solid-state laser engineering (Springer). https://books.google.com/books?hl=en&lr=&id=NtjqCAAAQBAJ&oi=fnd&pg=PA1&dq=Koechner+W.+(2013).+Solid+-+state+laser+engineering&ots=SkB1rEC5Fk&sig=avp79I09ulpXDCE-eYoFnUm0qsI#v=onepage&q=Koechner%20W.%20(2013).%20Solid%20-%20state%20laser%20engineering&f=false
61. Catlow C. R. A., Chadwick A. V., Corish J., et al. (1989). Defect structure of doped CaF_2 at high temperatures. *Phys. Rev. B* **39**:1897. DOI:10.1103/physrevb.39.1897

FUNDING AND ACKNOWLEDGMENTS

We would like to appreciate XAFS measurement provided by beamline BL11B of Shanghai Synchrotron Radiation Facility, and User Experiment Assist System of Shanghai Synchrotron Radiation Facility. We would like to thank Dr. Meng Wang from Shanghai Institute of Microsystem and Information Technology for providing the XANES spectra calculations and discussions. We are grateful to the staff members of the general purpose powder diffraction (https://csns.cn/31113.02.CSNS.GPPD) and the energy-resolved neutron imaging instrument (https://csns.cn/31113.02.CSNS.ERNI) at the China Spallation Neutron Source (https://csns.cn/31113.02.CSNS), for providing technical support and assistance in data collection and analysis. This work has been financially supported by Natural Science Foundation of China (61925508, 62475104), CAS Project for Young Scientists in Basic Research (YSBR-024), Guangdong Basic and Applied Basic Research Foundation (2023A1515011105). The funders had no role in study design, data collection and analysis, decision to publish, or preparation of the manuscript.

AUTHOR CONTRIBUTIONS

L.S., F.M. and J.C. conceived the project. J.L., F.M. and J.Y. wrote the article and were primarily responsible for the experiment and calculation. J.Y., J.L. and F.M. were responsible for the NPD measurement and analysis. H.W., Z.Z. and D.J. carried out the XAFS measurement and analysis. Z.Z., Y.X., H.W., D.J. and Q.W. grew the crystals. Y.X. and Z.Z. carried out the absorption measurement and analysis. All authors contributed to the general discussions.

DECLARATION OF INTERESTS

The authors declare no competing interests.

DATA AND CODE AVAILABILITY

Data are available from the corresponding author upon reasonable request.

SUPPLEMENTAL INFORMATION

It can be found online at https://doi.org/10.59717/j.xinn-mater.2026.100217.